J Adv Ceram

Research Article

Combining multiple strategies for fast densification and superior mechanical properties in 8YSZ with cold sintering pre-treatment

Sung-Hyun Kim[1,†], Sevag Momjian[2,3,†], Sang-Min Hong[1], Jong-Won Kim[1], Ha-Jin Gu[1], Young-Jae Kim[1], Ah-Hyeon Park[1], Muhammad Uzair[1], Pathan Sharief[1], Jeong-Min Park[4], Chung-Soo Kim[4], Kyung-Seok Moon[5], Jing Guo[6,✉], Clive A. Randall[2,3,✉], Sang-Chae Jeon[1,✉]

Cite this article: Kim S-H, Momjian S, Hong S-M, et al. *J Adv Ceram* 2026, **15**(5): 9221278. https://doi.org/10.26599/JAC.2026.9221278

ABSTRACT: The cold sintering process (CSP), which has recently attracted significant research attention, is an emerging technique that enables the densification of high-melting-point ceramics at temperatures far lower than those required for conventional sintering (CS) by utilizing solvent-assisted mechanisms. In this study, CSP is employed as a pretreatment strategy for 8 mol% yttria-stabilized zirconia (8YSZ) to modify the initial microstructural and interfacial state prior to high-temperature sintering. In parallel, Fe_2O_3 was introduced as a sintering aid to enhance grain-boundary diffusion during the high-temperature stage. Rather than acting as an independent densification step, CSP establishes a path-dependent initial condition that governs the subsequent densification trajectory during conventional sintering. CSP at 180 °C for 1 h under a uniaxial pressure of 200 MPa, followed by postannealing at 1200 °C for 30 min, resulted in a high relative density of 98.11% theoretical density (TD). Depending on the type of solvent, the treated samples exhibited either a high Vickers hardness (H_v = 14.99 GPa) or a high fracture toughness (K_{IC} = 5.56 MPa·m$^{1/2}$), reflecting differences in grain growth mode and crack-path geometry. Stage-resolved densification kinetics were directly monitored using laser dilatometry, enabling the identification of pressure-driven rearrangement, solvent-mediated consolidation, and thermally activated diffusion contributions. The results demonstrate that CSP pretreatment governs the particle packing topology and interfacial chemistry, while Fe_2O_3 addition primarily amplifies high-temperature grain-boundary diffusion. This sequential coupling establishes a mechanistic framework for path-dependent densification in CSP-assisted ceramic processing.

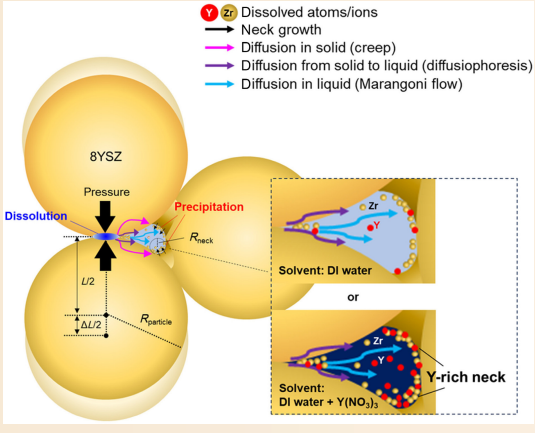

KEYWORDS: cold sintering; 8 mol% yttria-stabilized zirconia (8YSZ); densification; mechanical property

1 Introduction

8 mol% yttria-stabilized zirconia (8YSZ) is an important functional ceramic material utilized in various applications, such as cutting tools, oxygen sensors, thermal barrier coatings (TBCs), solid oxide fuel cells (SOFCs), and transparent ceramics. This is due to its remarkable properties, including high wear resistance, thermal stability, excellent chemical inertness, stability at high temperatures, high ionic conductivity, and a high refractive index [1–11]. However, conventional sintering (CS) of 8YSZ generally requires temperatures above 1400 °C to achieve a relative density of ≥ 95% [12–16]. To reduce the sintering temperature, various dopants, such as SiO_2 [17,18], NiO [19], MnO_2 [20], and Fe_2O_3 [21,22], have been incorporated into 8YSZ. Among them, Fe_2O_3 has been shown to achieve ~96% of the theoretical density (TD) at a reduced sintering temperature of 1150 °C. In addition to dopant incorporation, several advanced sintering techniques have been explored to promote the densification of 8YSZ ceramics, including

† Sung-Hyun Kim and Sevag Momjian contributed equally to this work.

[1] School of Materials Science and Engineering, Changwon National University, Gyeongsangnam-do 51140, Republic of Korea. [2] Department of Materials Science and Engineering, The Pennsylvania State University, PA 16802, USA. [3] Materials Research Institute, The Pennsylvania State University, PA 16802, USA. [4] Analysis & Certification Center, Korea Institute of Ceramic Engineering and Technology, Gyeongsangnam-do 52851, Republic of Korea. [5] School of Materials Science and Engineering, Gyeongsang National University, Gyeongsangnam-do 52828, Republic of Korea. [6] State Key Laboratory for Mechanical Behavior of Materials, School of Materials Science and Engineering, Xi'an Jiaotong University, Xi'an 710049, China.

✉ Corresponding authors. E-mail: J. Guo, jingguo19@xjtu.edu.cn; C. Randall, car4@psu.edu; S.-C. Jeon, scjeon@changwon.ac.kr

Received: December 30, 2025; Revised: February 12, 2026; Accepted: March 8, 2026

© The Author(s) 2026. This is an open access article under the terms of the Creative Commons Attribution 4.0 International License (CC BY 4.0, http://creativecommons.org/licenses/by/4.0/).

hot isostatic pressing (HIP) [11,23], microwave sintering (MVS) [13,24], spark plasma sintering (SPS) [12,25,26], and flash sintering [27,28]. However, these processes often require specialized equipment, significant energy input, and incur high operational costs, thereby limiting their widespread application. 8YSZ is known to be stabilized in the fluorite cubic structure at room temperature due to the high Y_2O_3 content [29,30], which provides high oxygen-ion conductivity and structural stability.

Meanwhile, the cold sintering process (CSP) has been recognized as a viable technique for achieving densification of ceramic materials at extremely low temperatures (< 300 °C) through the combined action of a transient solvent and applied pressure [31–37]. In addition to lowering sintering temperatures and thereby reducing energy consumption, the low-temperature nature of CSP may enable more precise control over the microstructures and properties of ceramics. When CSP alone yields sufficient densification, it can serve as a direct alternative to conventional sintering [31–35]. However, for materials with high melting points or in cases where the solvent contribution is minimal, CSP can be employed as a pretreatment step prior to high-temperature sintering to facilitate densification [36,38,39]. This is because CSP pretreatment can promote initial densification prior to conventional sintering, thereby significantly lowering the subsequent sintering temperature. Guo *et al.* [40–42] demonstrated that applying CSP as a pretreatment for materials such as $BaTiO_3$ and YSZ resulted in a reduction of the following sintering temperature by approximately 300 °C. Similarly, Ullah *et al.* [43] reported that CSP pretreatment in $BaTiO_3$ enhanced the final sintered density by 36.3% TD compared to the untreated counterpart. As the sintering temperature decreases, the grain growth rate is suppressed, which helps prevent the formation of abnormal grains and enables the development of finer microstructures. The benefits of CSP pretreatment become even more pronounced when it is necessary to avoid the formation of high-temperature-induced secondary phases or to precisely control the grain size. In YSZ research, various efforts have been made to enhance the densification kinetics during CSP pretreatment, such as adjusting the pH of the solvent [44], adding Fe_2O_3 as a dopant, and using reactive hydroxide precursors [21,22,44,45]. According to Huang *et al.* [44], the total amount of Y^{3+} and Zr^{4+} ions dissolved into the solvent during CSP was highest under acidic conditions. However, under neutral pH, the ratio of dissolved Y^{3+} to Zr^{4+} was significantly higher (~45), which led to the most favorable densification behavior during the subsequent sintering step. This effect has been attributed to enhanced diffusion associated with Y incorporation under acidic conditions.

The advantages of CSP are primarily attributed to its ability to achieve densification at low temperatures. Accordingly, a comprehensive understanding and effective control of the densification behavior are essential to fully realize the potential of CSP. To analyze such densification behavior, previous studies have employed digital contact sensors to monitor shrinkage behavior under various heating rates [46]. By applying the constant heating rate (CHR) method, the activation energy for densification was calculated and found to be significantly lower than that of conventional sintering [47]. Densification during CSP involves a sequence of pore elimination mechanisms, including particle deformation under pressure (compaction and capping), solvent-assisted particle rearrangement (consolidation or sliding), and diffusion-driven final pore removal and fluid extraction under combined temperature and pressure conditions [48]. While a deep understanding of the densification mechanism benefits from the ability to independently examine the effects of key variables such as pressure, solvent, and temperature, most prior studies have observed the effects of multiple processing parameters simultaneously. As a result, it has been difficult to isolate the individual contributions of each parameter to the overall densification behavior.

In this study, an *in situ* laser dilatometer, which can be installed in a commercial furnace without any equipment modification, was employed to monitor the shrinkage behavior specifically during the CSP stage under the sequential application of pressure and temperature. This experimental design enables the stagewise resolution of variable effects within CSP by first observing pressure-driven densification and subsequently identifying temperature-assisted contributions. Accordingly, densification occurring at low temperature prior to CS can be directly quantified. However, although pressure and temperature contributions can be experimentally resolved during CSP, the overall CSP → CS route is interpreted here as a path dependent, sequentially coupled process rather than a set of independent densification steps. The geometric packing state and interfacial chemistry established during CSP are inherited as the initial conditions for the subsequent high-temperature sintering stage. Within this framework, $Y(NO_3)_3{\cdot}6H_2O$ was used as a solvent to create an acidic environment, thereby increasing the dissolution of Y^{3+} and Zr^{4+} ions [44] while also serving as an additional Y source that increases the Y^{3+}/Zr^{4+} ratio. In parallel, Fe_2O_3 was introduced as a sintering aid whose primary influence manifests during the subsequent high-temperature sintering stage through enhanced grain-boundary diffusion. These factors therefore act predominantly at different stages of the densification pathway yet remain sequentially coupled through inheritance of the CSP-established microstructural state.

The *in situ* shrinkage measurements demonstrate that measurable densification occurs during the CSP stage prior to heating to 1200 °C, confirming that CSP modifies the starting microstructural state rather than acting merely as a precursor to conventional sintering. The densification behavior during the high-temperature stage is interpreted based on the inherited state and the resulting final density and microstructure. Beyond densification enhancement, this work establishes a microstructure–property control framework in which solvent chemistry during CSP governs grain growth mode and crack-path topology, thereby enabling controlled tuning of the hardness–toughness balance while reducing the required high-temperature sintering duration.

2 Experimental

All specimens used in this study were prepared from commercial 8 mol% YSZ powder (99.9% purity, 20–40 nm, NP-40082-C, MSE Supplies, USA). The powder was used as received without additional phase pretreatment. To evaluate the effect of Fe addition, high-purity Fe_2O_3 powder (99.995% purity, No. 529311, Aldrich Prod., USA) was added at 4 wt%. The Fe_2O_3 content was fixed at 4 wt% based on previous reports using similar CSP-assisted sintering routes, where this concentration provided near-optimal densification among the tested compositions [22]. The powder mixture was homogenized by ball milling for 24 h in high-purity ethanol (99.9% purity, Samchun Chemical, Republic of Korea) as the dispersing medium. Following the mixing step, ethanol was evaporated on a hot plate, and the resulting powder was further dried in a convection oven at 80 °C for 24 h to ensure complete removal of residual moisture. The agglomerated powder was then manually crushed using an agate mortar and sieved to a particle size below 63 μm. For the CSP, the solvent was added at a ratio of 20 wt% relative to the sieved powder. Deionized (DI) water or a $Y(NO_3)_3$ solution was used as the solvent. The $Y(NO_3)_3$

solution was prepared by dissolving $Y(NO_3)_3{\cdot}6H_2O$ hydrate (99.99% purity, Samchun Chemical, Korea) in DI water to a concentration of 2 mol·L^{-1}. The reported pH of this solution is 3.5 (at 20 °C, 50 g·L^{-1} in H_2O). The theoretical pH of the 2 mol·L^{-1} solution was calculated based on the hydrogen ion concentration using Eq. (1), resulting in a value of 2.315:

$$\mathrm{pH} = -\log\left(\mathrm{H}^+\right) \tag{1}$$

The prepared solvent was added to the sieved powder at a ratio of 20 wt% and mixed in a mortar for more than 5 min to ensure uniform wetting. The wet powder mixed with the solution was loaded into a 12.7 mm diameter cylindrical mold and compacted using a 40-ton laboratory press equipped with a programmable electric hydraulic pump (YLJ-40TA-PE, MTI Co., USA). The compaction process consisted of two steps: Uniaxial pressure of 200 MPa was applied at room temperature for 10 min, followed by cold sintering at 200 MPa and 180 °C for 1 h. During the CSP process, the heating and cooling rates were maintained at 9 °C·min^{-1}. To prepare two specimens simultaneously, a middle punch was inserted between powder layers in the mold. After cold sintering, the diameter, height, and weight of each pellet were measured to calculate the bulk density. To perform *in situ* monitoring of the densification behavior during CSP, a laser dilatometer (LS-9120MT & LS-9120MR, KEYENCE, Japan) was installed laterally to the CSP setup to measure the specimen shrinkage measured through the mold throughout the process (Fig. S1 in the Electronic Supplementary Material (ESM)). Subsequently, all specimens processed by CSP were subjected to CS in air using a box furnace at 1200 °C for 30 min. The heating and cooling rates were maintained at 5 °C·min^{-1}. The relative density was calculated using Archimedes' method. For Fe_2O_3-free samples, a TD of 6.00 g·cm^{-3} was used for 8YSZ. For the 4 wt% Fe_2O_3-doped samples, the TD was calculated using the rule of mixtures, considering densities of 6.00 g·cm^{-3} for 8YSZ and 5.24 g·cm^{-3} for Fe_2O_3.

In this study, the CSP specimens were designated according to their processing conditions as follows: 8YSZ processed with DI water (8YSZ-D), 8YSZ with 4 wt% Fe_2O_3 processed with DI water (4Fe-8YSZ-D), and 8YSZ with 4 wt% Fe_2O_3 processed with $Y(NO_3)_3$ solution (4Fe-8YSZ-Y). These abbreviations are used throughout this paper to refer to each specimen. Figure 1 represents the manufacturing process of the samples utilized in this research.

The diffraction patterns of the crystalline phases in the specimens were obtained by X-ray diffraction (XRD) and analyzed using Jade software (version 6, Materials Data Inc., USA) and Rietveld refinement. XRD was performed on the CS-treated bulk samples after mechanical polishing. Sintered specimens were cut with a diamond saw to expose the internal cross-sections, followed by surface polishing and thermal etching. The grain and grain boundary structures were then examined using a scanning electron microscope (SEM; MIRA I, TESCAN, Czech Republic). An X-ray photoelectron spectrometer (XPS; AXIS SUPRA+, Kratos Analytical Ltd., UK) was employed to analyze the near-surface O 1s chemical states of the sintered specimens. The deconvoluted components were used to compare relative changes in lattice oxygen and defect/hydroxyl-related oxygen species among samples rather than to quantify bulk oxygen vacancy concentrations. Vickers hardness measurements (HV-100, Mitutoyo, Japan) were performed under a load of 19.61 N (2 kgf) for 10 s, with more than eight indentations evaluated for each specimen. The lengths of radial cracks generated during indentation were measured from SEM images, and the fracture toughness (K_{IC}) of each sample was calculated using the indentation fracture resistance model of Anstis *et al.* [11]. A Talos F200X transmission electron microscope (Thermo Fisher Scientific, USA) was used. A Helios G4 DualBeam FIB system (Thermo Fisher Scientific, USA) was used for TEM sample preparation, and the grain boundary segregation of yttrium was analyzed as a function of solvent type.

3 Results and discussion

Before discussing the experimental results, we clarify that the present study was designed as a sequential, path-dependent processing strategy (CSP → CS) rather than a factorial, variable-isolating investigation. Prior studies have shown that Fe_2O_3 primarily influences densification during the high-temperature sintering stage via grain-boundary chemistry and diffusion kinetics, whereas CSP pretreatment affects the low-temperature stage by modifying particle packing and contact evolution under pressure in the presence of a transient solvent. Accordingly, these mechanisms operate at distinct stages of the densification pathway but remain sequentially coupled: The microstructural and interfacial state established during CSP is inherited by the subsequent CS stage, effectively serving as the initial condition for final densification.

The enhanced densification observed here can thus be understood through a sequential, stage-resolved framework rather than a single dominance of Fe_2O_3-addition. CSP primarily affects

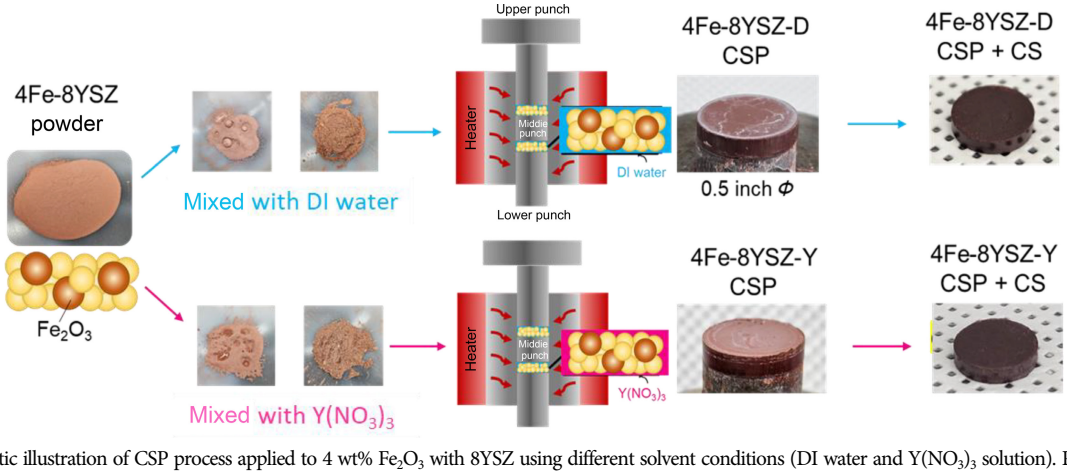

Fig. 1 Schematic illustration of CSP process applied to 4 wt% Fe_2O_3 with 8YSZ using different solvent conditions (DI water and $Y(NO_3)_3$ solution). Process includes powder mixing, CSP, and CS.

清華大学出版社 Tsinghua University Press | SciOpen

the low-temperature packing stage, increasing the green density to ~59% via pressure-assisted particle rearrangement, a state unattainable by conventional compaction (~47%) [22]. This geometric advantage provides a densification "head start" prior to thermal activation. The stage separation is directly supported by *in situ* shrinkage measurements, which show measurable densification during the CSP stage before the 1200 °C CS step. During the subsequent high-temperature stage, Fe_2O_3 mainly contributes by activating grain-boundary diffusion and mass transport.

The synergistic nature of this sequence is supported by literature comparisons: With Fe_2O_3 addition alone, conventional sintering can achieve high density (e.g., ~95.2% TD at 1150 °C), whereas the sequential CSP–CS route reaches a comparable density at a lower temperature (e.g., ~95.8% TD at 1100 °C) under otherwise similar processing logic [22]. This indicates that CSP-enabled packing and interfacial modification provide a densification "head start" that reduces the thermal budget required for near-full densification, while Fe_2O_3 primarily amplifies grain-boundary transport once thermally activated. Therefore, the improved final density and mechanical performance arise from complementary, sequential contributions rather than a redundant effect.

Figure 2(a) shows the XRD patterns of the starting powder and the CSP and CS-treated samples. As magnified in Figs. 2(b) and 2(d), the fluorite/cubic structure observed in the as-prepared 4Fe-8YSZ powder (I) was largely retained after CSP and subsequent CS at 1200 °C for 30 min (II–V), indicating that the cubic matrix remains the dominant phase. The absence of clear splitting of peaks in the high-angle (400) reflection in Fig. S2 in the ESM also indicates that the matrix is best described as fluorite/cubic-stabilized YSZ rather than a distinct tetragonal phase. This assignment is further supported by the Rietveld refinement (Fig. S3 and Table S1 in the ESM), which identifies the dominant matrix as fluorite/cubic 8YSZ within the resolution of the analysis. It should be noted that the commercial 8YSZ nanopowder used in this study (NP-40082-C, 20–40 nm) exhibits size-dependent crystallographic characteristics. Such nanosized zirconia powders may contain surface/strain-induced monoclinic ZrO_2 (m-ZrO_2) that differs from those of bulk-stabilized zirconia. In nanoscale systems, surface energy, residual strain, and particle-size effects are known to shift phase stability boundaries, allowing a monoclinic contribution even in nominally 8 mol% YSZ compositions. Therefore, the detection of monoclinic-related reflections after ball milling and CSP does not indicate bulk phase instability but reflects the intrinsic strain- and size-sensitive nature of the nanopowder system. This interpretation is consistent with previous reports showing that mechanical processing can increase monoclinic fractions in nanoscale YSZ, which are typically restabilized during subsequent high-temperature sintering [49].

Although bulk 8YSZ is thermodynamically stabilized in the cubic fluorite field, weak monoclinic signatures can occasionally be detected in nanocrystalline specimens due to surface/strain effects. Accordingly, the residual monoclinic-related peaks after sintering are attributed to surface-localized cubic → monoclinic transformation induced during mechanical handling and polishing [49] rather than bulk phase instability. Given the high relative density of the sintered bodies and the ZrO_2–Y_2O_3 phase diagram, the bulk of the sintered specimens is considered to consist predominantly of a stabilized cubic solid solution [41]. Furthermore, as shown in Figs. 2(c) and 2(e), the hexagonal Fe_2O_3 phase (H-Fe_2O_3) present in the starting powder remained after CSP but was no longer detected after sintering.

Figure 3 shows the temperature and pressure profiles, along with the associated shrinkage behavior of 8YSZ powder during CSP, in which 20 wt% DI water was used as the solvent. The pellet height was continuously monitored using the laser dilatometer setup described in Fig. S1 in the ESM, enabling *in situ* analysis of densification behavior throughout the CSP process. Figure 3(a) illustrates the overall shrinkage behavior occurring throughout the CSP process, with each segment labeled numerically from 1 to 4. Figure 3(b) highlights the transition from section 1 to section 2, which corresponds to the initial stage of CSP, during which the applied pressure increases to 200 MPa over the course of 1 min. Similar to the early stage of conventional uniaxial pressing, particles displaced from the punch surface infiltrate nearby voids, initiating macroscopic rearrangement near the punch region. However, in CSP, the presence of the solvent promotes enhanced particle sliding, leading to a shrinkage of approximately 2.22 mm as the pressure reaches 200 MPa. Figure 3(c) presents the shrinkage behavior observed during section 2 to section 3, corresponding to the 10 min period in which the pressure is maintained at 200 MPa. During this stage, the solvent migrates through interparticle voids, facilitating more uniform particle rearrangement within the mold.

In addition, localized contact deformation occurs under sustained high pressure. The stepwise nature of the shrinkage curve is attributed to the periodic loading inherent to the mechanical operation of the equipment. Most of the shrinkage occurs during section 1-2 (the specific time range between number 1 and 2) and is primarily attributed to interparticle slip and rearrangement. In section 2-3, additional densification occurs

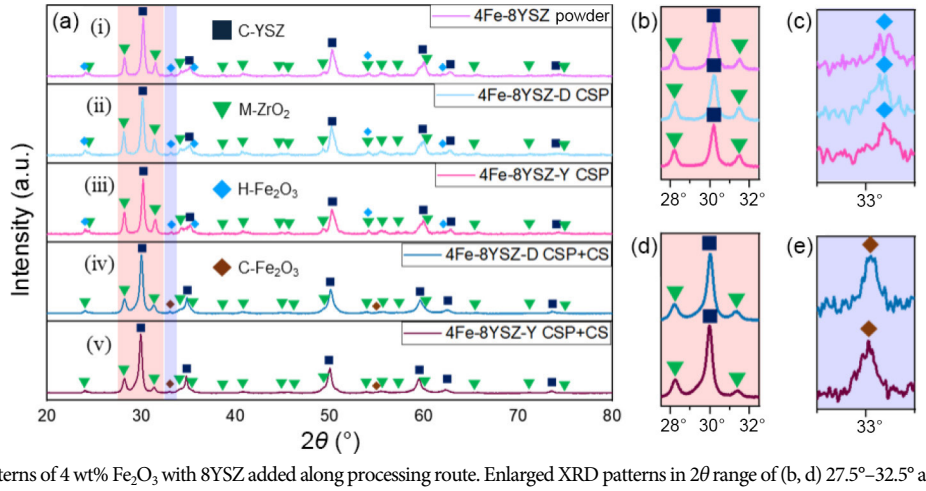

Fig. 2 (a) XRD patterns of 4 wt% Fe_2O_3 with 8YSZ added along processing route. Enlarged XRD patterns in 2θ range of (b, d) 27.5°–32.5° and (c, e) 32.5°–33.5°.

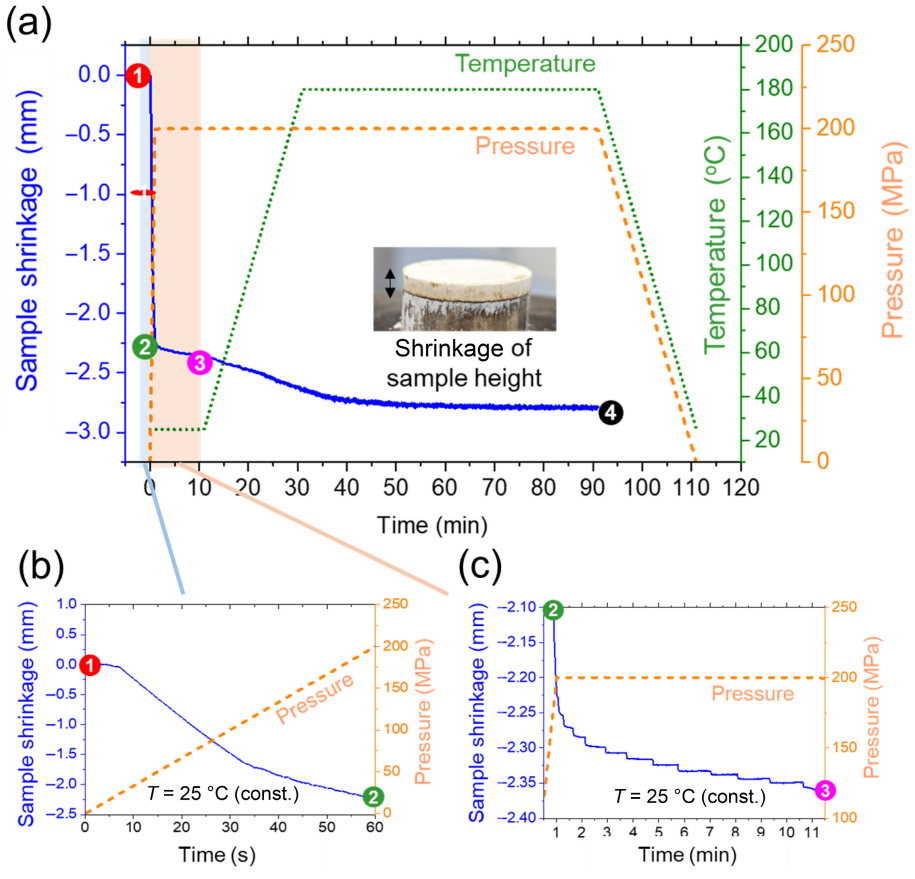

Fig. 3 (a) Shrinkage behavior of pure 8YSZ-D during CSP process under controlled pressure and temperature conditions (absolute displacement, mm). Enlarged view of shrinkage behavior (b) from point 1 to point 2 during pressure ramp-up and (c) from point 2 to point 3 during 10 min pressure holding stage at 200 MPa.

due to residual rearrangement and localized contact deformation of the particles. While both sections involve shrinkage under externally applied pressure, separating them allows for a clearer analysis of how individual processing parameters contribute to densification. This distinction also provides a basis for evaluating which solvent is more effective in each stage of the densification process during CSP. Based on this stage-resolved CSP shrinkage framework, we next compare solvent-dependent densification behavior in Fe_2O_3-added specimens and quantify diffusion-assisted contributions during the heating/isothermal segments.

Figure 4 compares the segment-wise shrinkage behavior of 4Fe-8YSZ specimens during CSP, depending on the type of solvent, following the same framework as described in Fig. 3. Figures 4(a) and 4(b) illustrate the shrinkage response during section 2-3, where pressure is the dominant factor, while Figs. 4(d) and 4(e) show the behavior in section 3-4, where both pressure and temperature are applied. For clarity, the overall shrinkage process is simplified using a two-particle model, with L, L_0, and ΔL (a difference between L and L_0) indicated along the y-axis. The initial length L_0 was defined at the moment when the applied pressure reached the target high-pressure level (position 2 in Fig. 3), after seating of the paste and establishment of stable punch–specimen contact. At this stage, the specimen behaves as a mechanically coherent pellet with a well-defined geometry. Any displacement occurring before this point, associated with paste accommodation and die filling, was excluded from the densification analysis. In both Figs. 4(a) and 4(d), the sample prepared with $Y(NO_3)_3$ solution (4Fe-8YSZ-Y) shows greater shrinkage than that prepared with DI water (4Fe-8YSZ-D). This indicates that $Y(NO_3)_3$ promotes both particle rearrangement via slip and deformation (Fig. 3(b)) and densification by diffusion (Fig. 4(e)). Notably, 4Fe-8YSZ-Y exhibits more pronounced stepwise shrinkage behavior, as seen in the enlarged view in Fig. 4(a), and a larger normalized shrinkage in Fig. 4(d) further supports this trend. As a cumulative result, the total shrinkage ratio after CSP was 19.1% for 4Fe-8YSZ-D and 31.3% for 4Fe-8YSZ-Y, confirming a significant difference. In the particle arrangement stage, solvent penetration is important, so we compared the wetting angles of the two solvents used in this experiment (Fig. S4 in the ESM). At room temperature, DI water exhibits a significantly lower wetting angle, suggesting that penetration between YSZ particles is relatively easy, whereas the $Y(NO_3)_3$ solution has a larger wetting angle. From the perspective of the wetting angle, penetration between particles is minimal, so it is expected that the $Y(NO_3)_3$ solution does not contribute to particle sliding; however, under high pressure, the wetting angle effect is not significant. It should be noted that solvent penetration between particles during the early CSP stage is governed by capillary-driven infiltration. The driving pressure for penetration can be approximated as Eq. (2) [50]:

$$P_{\text{capillary}} = \frac{2\gamma\cos\theta}{r} \tag{2}$$

where γ is the liquid surface tension, θ is the wetting angle, and r is the characteristic pore radius between particles. Although DI water shows a lower contact angle at room temperature (Fig. S4 in the ESM), the external uniaxial pressure during CSP (hundreds of MPa) far exceeds the capillary driving pressure, making solvent transport primarily pressure-driven rather than wetting-limited. Moreover, the $Y(NO_3)_3$ solution rapidly infiltrates the compact upon heating (~150 °C), indicating that interfacial chemistry rather than ambient wetting dominates the solvent effect under

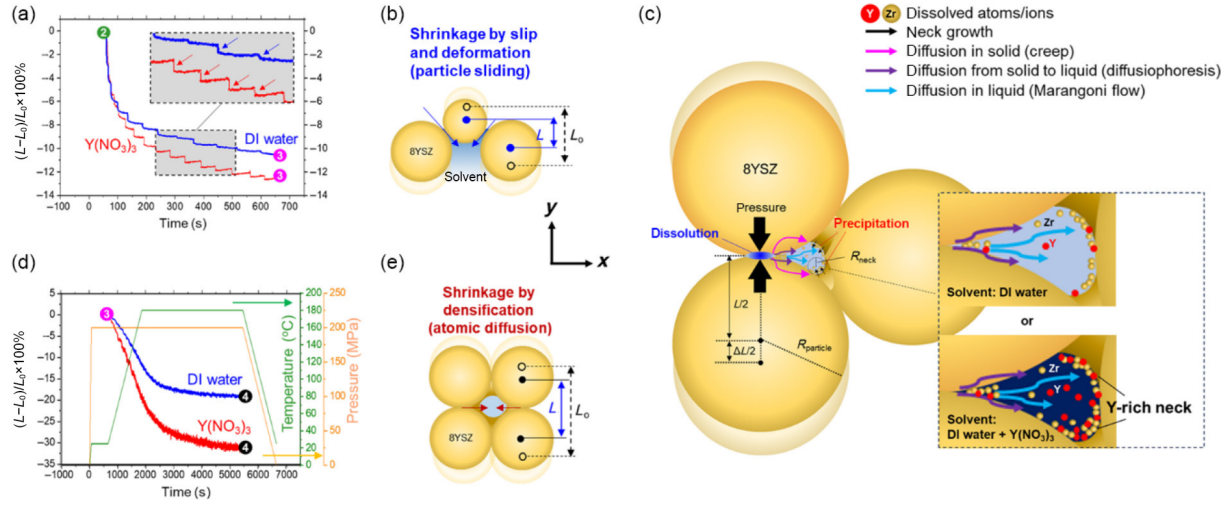

Fig. 4 (a) Shrinkage (%) of 4Fe-8YSZ-D (blue) and 4Fe-8YSZ-Y (red) during pressure holding stage (normalized linear strain, $\Delta L/L_0 \times 100\%$). (b) Schematic illustration of particle rearrangement occurring during pressure holding stage in (a). (c) Schematic of dissolution and precipitation of yttria versus pH of solvent (DI water and $Y(NO_3)_3$ + DI water) during CSP. (d) Shrinkage (%) of 4Fe-8YSZ-D (blue) and 4Fe-8YSZ-Y (red) during heating and temperature holding stage under constant pressure (normalized linear strain). (e) Schematic illustration of particle densification occurring during thermal stage in (d).

CSP conditions. Instead, in the case of the $Y(NO_3)_3$ solution, chemical reactions are active on the YSZ particle surface, causing Y and Zr ions to dissolve well, resulting in visible local particle rearrangement throughout the specimen. Considering that the pH of the $Y(NO_3)_3$ solution is in the acidic range and previous results [44] observed the dissolution behavior of YSZ at room temperature, the solvent effect of the $Y(NO_3)_3$ solution shown in Fig. 4(a) is due to chemical action. Furthermore, when measuring the wetting angle as the temperature increased, it was observed that the $Y(NO_3)_3$ solution was completely absorbed into the YSZ specimen within a few seconds at approximately 150 °C (Figs. S4(b) and S4(d) in the ESM). Therefore, it is considered that the wetting angle effect of the solvent on the densification behavior during CSP is not significant. Figure 4(d) presents the shrinkage behavior of the specimens measured during the heating stage, where the temperature was increased to 180 °C at a rate of 9 °C·min^{-1} while maintaining the applied pressure at 200 MPa, followed by a 1 h hold. To distinguish the shrinkage associated with different densification mechanisms, the data were normalized using section 3 from Fig. 3(a) as the point at which initial compaction was nearly complete, and this point is labeled as 3 in Fig. 4(d). As the temperature increases, atomic diffusion is activated, leading to the formation of necks and closer packing of particles, which results in significant shrinkage (Fig. 4). The kinetics of diffusion-based densification vary depending on the type of solvent, and this ultimately determines the final density of the specimens after CSP. Figure 4(c) presents a schematic illustration of the material transport pathways occurring between particles during the CSP, and the associated transport mechanism is further described in Fig. S5 in the ESM. In regions where the compressive stress is concentrated between particles, dissolution (atom detachment) occurs, followed by atom transport through a fast diffusion path, namely, the liquid phase, and subsequent precipitation (atom attachment) onto the neck surfaces where the pressure is relatively low. This process proceeds in a serial manner, and the slowest step among them determines the overall rate. Transport through the transient liquid can be rationalized by coupled concentration-driven diffusion in the solution and interfacial mass transfer; additional flow-assisted contributions may also occur depending on local gradients and wetting dynamics [51]. This approach provides a kinetics-based framework for identifying rate-controlling steps in the densification process, thereby offering guidance for future material and process design strategies aimed at accelerating densification and lowering the energy input into ceramic sintering. In this study, the use of a laser dilatometer enabled real-time monitoring of shrinkage during CSP, allowing for a quantitative analysis of the densification mechanism. This method further facilitates a detailed assessment of how solvent selection and process parameters influence the overall densification behavior.

In consideration of the above and the multiple-mechanism stepwise nature of the densification process, the CHR method is used to determine the energetics related to the initial diffusional driven particle rearrangement stage during heating. This is shown in Fig. 5(a), where the strain multiplied by the temperature is plotted on a logarithmic scale against the inverse of temperature. The initial steep rise in the first 20 °C is controlled by particle slip and localized contact deformation. From 75 °C onward, a linear region is observed for both the DI water and $Y(NO_3)_3$ cases. During this portion of densification, the diffusional transport mechanism drives shrinkage, as discussed earlier. The effective activation energy for this region can be determined following the procedures set by Young and Cutler [52,53]. When sintered with DI water, the effective activation energy was calculated to be 26.5±0.1 kJ·mol^{-1}. Indicative from the lower activation energies, the addition of water drives an aqueous diffusional mechanism, and the lower energy barrier for diffusion enables lower sintering temperatures. Upon the addition of $Y(NO_3)_3$, the activation energy decreased to 21.9±0.1 kJ·mol^{-1}. This agrees with previous observations, wherein the addition of $Y(NO_3)_3$ catalyzes the diffusional process and reaffirms the role of pH in modifying microstructural development under CSP conditions.

As the isothermal region remains linear in the CHR plot, the diffusion-based particle rearrangement stage extends into the isothermal regime. Within this stage, densification occurs through a liquid diffusion process. Following a previous report where the CSP of ZnO was modeled by a double relaxation [54], a similar approach is taken here. The double relaxation function is shown in Eq. (3):

$$g(t) = \varepsilon_f \left[A \exp\left(-\left(\frac{t}{\tau_1}\right)^{\beta_1} \right) + (1-A) \exp\left(-\left(\frac{t}{\tau_2}\right)^{\beta_2} \right) \right] \quad (3)$$

where ε_f is the final theoretical strain that the system will reach. A

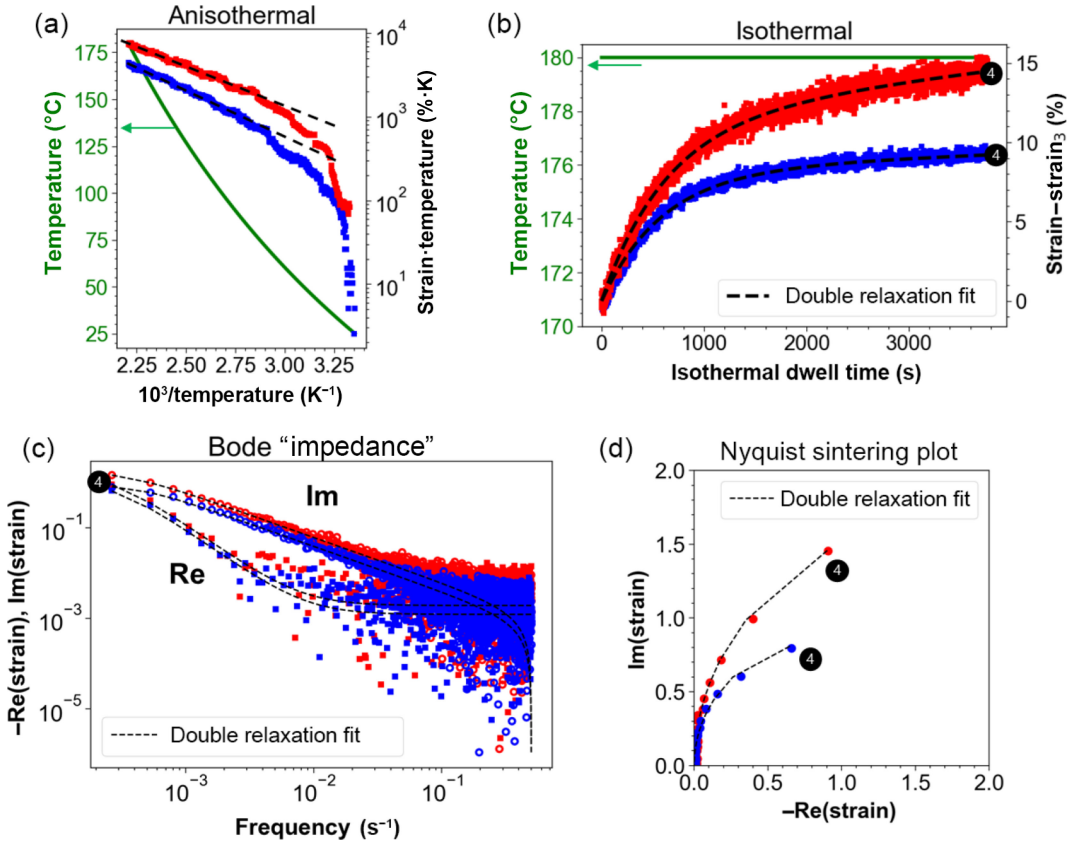

Fig. 5 (a) CHR plots of 4Fe-8YSZ-D (blue) and 4Fe-8YSZ-Y (red) during heating and temperature holding stage under constant pressure. Dashed lines (black) are linear fits. (b) Strain of 4Fe-8YSZ-D (blue) and 4Fe-8YSZ-Y (red) during temperature and pressure holding stage. Dashed lines (black) are respective double relaxation fits. (c) Bode strain (%) representation of 4Fe-8YSZ-D (blue) and 4Fe-8YSZ-Y (red) during temperature and pressure holding stage. Dashed lines (black) are respective double relaxation fits. (d) Complex plane strain representation of 4Fe-8YSZ-D (blue) and 4Fe-8YSZ-Y (red) during temperature and pressure holding stage. Dashed lines (black) are respective double relaxation fits.

is a weighting factor between the two relaxations, t is time, τ_1 and τ_2 are the respective relaxation times, and β_1 and β_2 are the respective stretching exponents. The application of Eq. (3), as a first-order approximation to the overall densification process despite the nonlinearity of the system, is valid, provided that the constituent relaxation times are sufficiently different. It had been previously observed that the double relaxation function is able to describe isothermal strain by superposition if the relaxation times are an order of magnitude apart. Here, the isothermal data are normalized to start from a final strain of zero, and Eq. (3) is fit to the isothermal strain regime. The values are reported in Table 1. The effective activation energies for the first relaxation determined from the CHR method are additionally reported.

The double relaxation functions fit well to the experimental data in the isothermal regime. Contrary to what was to be expected, for the first relaxation, the dissolution-driven particle rearrangement stage of densification DI water has a shorter relaxation time than that from the $Y(NO_3)_3$ solution. The smaller relaxation time can be easily explained by the fact that the densification driven by DI water is closer to completion than for $Y(NO_3)_3$ at the time when the isothermal region began. Observably, the additional second relaxation is greatly accelerated by the presence of $Y(NO_3)_3$, as its relaxation time is half that of just DI water. The incompleteness of densification from this sintering process is shown in the frequency and complex strain representation of the isothermal data. The methodology used to obtain this formulism is explained in [54]. The final fitted strain indicates that if a material is sintered for longer times, greater densification is achieved. In the case of the $Y(NO_3)_3$ solution, the total final strain from the isothermal region would be 23%. This is greater than the final strain from DI water of 15%. This underscores the necessity of $Y(NO_3)_3$ for achieving faster sintering rates and higher final densities and is consistent with previous discussions highlighting the mechanistic influence of $Y(NO_3)_3$.

Table 1 Activation energies for initial relaxation mechanism and additionally fitted double relaxation values

Transient phase	DI water	$Y(NO_3)_3$
E_a/n (kJ·mol^{-1}) (anisothermal)	26.5±0.1	21.9±0.1
A	0.46	0.52
τ_1 (s) (β_1)	588 (1)	612 (1)
τ_2 (s) (β_2)	2128 (1)	1057 (1)
ε_f (%)	15	23

Note: E_a is an activation energy, and n is a constant that depends on the diffusional mechanism for densification (i.e., grain boundary or bulk diffusion) [52].

Figure 6 presents the microstructural analysis of CSP-treated 4Fe-8YSZ-D and 4Fe-8YSZ-Y samples, including SEM, TEM, and TEM/energy dispersive spectroscopy (EDS) results. Figure 6(a) shows the sample fracture surface after CSP, as observed by SEM. Particle agglomeration is evident, while grain growth remains minimal. Fe_2O_3 particles are distinguishable due to their relatively large size. Figures 6(b) and 6(d) are TEM images, which reveal a similar microstructure to the SEM observations; the Fe_2O_3 particles are confirmed by selected area electron diffraction (SAED). The low-magnification EDS mapping in Figs. 6(c) and 6(e)

further show that Fe_2O_3 particles are uniformly distributed throughout the scanned area. In the EDS mapping results of the specimen prepared with the $Y(NO_3)_3$ solution, regions with relatively high yttrium concentrations were frequently observed, as indicated by the arrows, and these features appeared more often than in the 4Fe-8YSZ-D sample (Fig. 6(c)). Figure S6 in the ESM shows the TEM/EDS analysis of the CSP-treated 4Fe-8YSZ-D and 4Fe-8YSZ-Y specimens, revealing the relative distribution of yttrium between YSZ particles. The 4Fe-8YSZ-Y sample exhibited a higher concentration of interparticle yttrium compared to 4Fe-8YSZ-D, which is consistent with the results shown in Fig. 6(e). This indicates that, in addition to the Y^{3+} ions dissolved from the particles during CSP, the Y^{3+} ions supplied from the $Y(NO_3)_3$ solution contribute to the increased yttrium content in the 4Fe-8YSZ-Y sample.

Figure 7 presents the SEM/EDS microstructures of the 4Fe-8YSZ-D and 4Fe-8YSZ-Y samples after sintering at 1200 °C for 30 min, with the corresponding EDS data summarized in Table S2 in the ESM. Grain growth was more pronounced in the sample with higher yttrium content, which is attributed to yttrium-enhanced diffusion that promotes material transport between particles [22]. Meanwhile, Fe_2O_3 was initially added as a sintering additive uniformly distributed between YSZ grains, as confirmed by EDS mapping (as denoted by arrows in Figs. 7(a) and 7(d)).

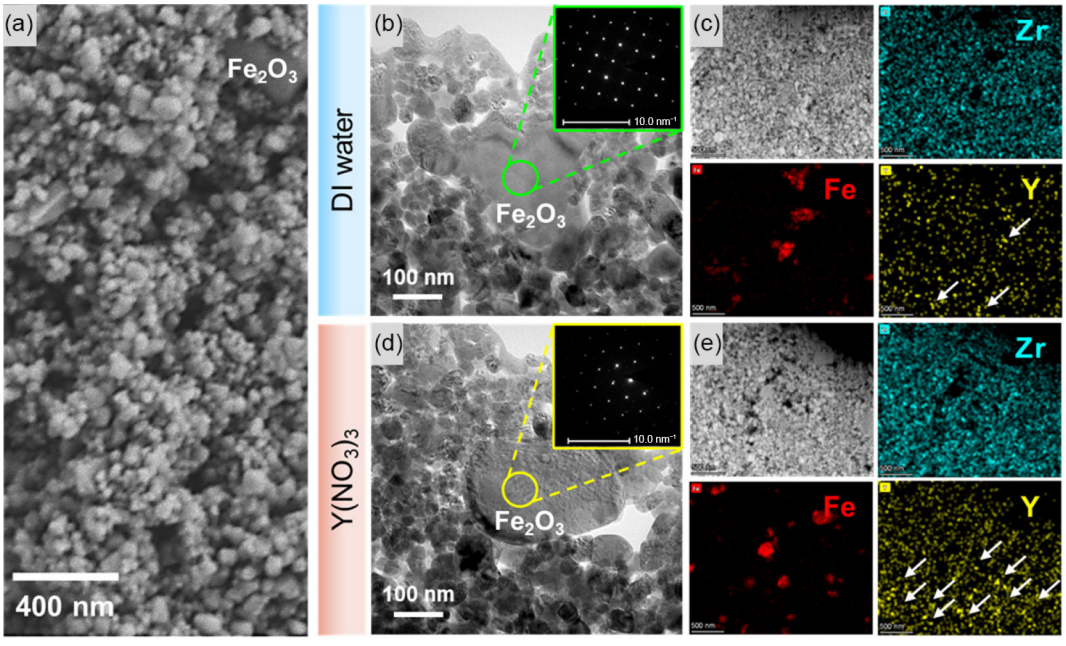

Fig. 6 (a) SEM image of fracture surface of CSP-processed 4Fe-8YSZ-Y pellet. (b) TEM image of CSP-processed 4Fe-8YSZ-D sample, along with SAED pattern of Fe_2O_3 obtained from region shown in TEM image. (c) TEM/EDS mapping of CSP-processed 4Fe-8YSZ-D sample. (d) TEM image of CSP-processed 4Fe-8YSZ-Y sample, along with SAED pattern confirming Fe_2O_3 secondary phase from indicated region in TEM image. (e) TEM/EDS mapping of CSP-processed 4Fe-8YSZ-Y sample (scale bars indicate 500 nm).

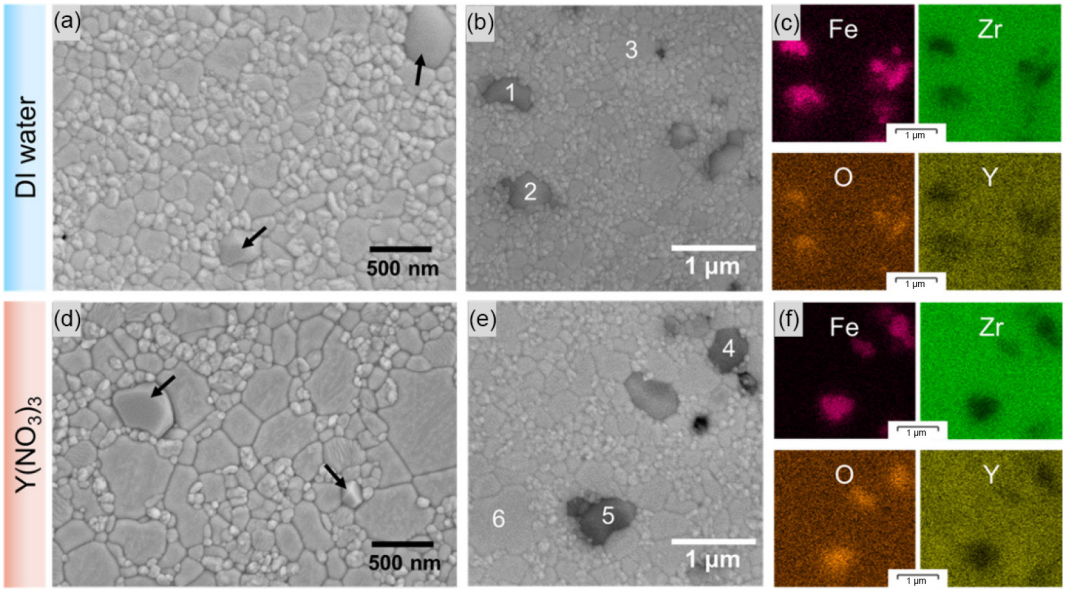

Fig. 7 (a) SEM micrograph of 4Fe-8YSZ-D sample sintered at 1200 °C for 30 min. Arrows indicate Fe-rich secondary phase. (b, c) SEM/EDS analysis of sample shown in (a). (d) Microstructure of 4Fe-8YSZ-Y sample sintered at 1200 °C for 30 min. Arrows indicate Fe-rich secondary phase. (e, f) SEM/EDS analysis of sample shown in (d), where regions 4 and 5 correspond to iron oxide and region 6 corresponds to YSZ matrix.

The incorporation of both yttrium and Fe_2O_3 also affected the final density of the specimens after CSP. Figure S7 in the ESM compares the green density (prepared by uniaxial pressing or CSP) and the relative density after sintering at 1200 °C for various specimens: uniaxially pressed 8YSZ, 8YSZ-D, 4Fe-8YSZ-D, and 4Fe-8YSZ-Y. The standard deviations of the measured values are summarized in Table S3 in the ESM. In terms of green density, the effects of CSP treatment, Fe_2O_3 addition, and the use of $Y(NO_3)_3$ solution are represented as effects ①, ②, and ③, respectively, enabling a stepwise evaluation of each parameter. This progressive increase in density is also reflected in the relative densities after sintering at 1200 °C for 30 min and 1 h, with both 4Fe-8YSZ-D and 4Fe-8YSZ-Y reaching values above 98% of the relative density. After sintering for 2 h at 1200 °C, even the uniaxially pressed 8YSZ and 8YSZ-D samples achieved relative densities of ~95%. These results clearly demonstrate that CSP treatment prior to sintering enhances densification kinetics and that Fe_2O_3 acts as an effective sintering aid [21,22], reducing the required sintering time while improving the final density. Previous studies [21,22] suggest that Fe-containing species can modify defect chemistry and enhance grain-boundary diffusion kinetics in YSZ systems.

Figure 8 presents the TEM images and XPS results of the 4Fe-8YSZ-D and 4Fe-8YSZ-Y samples after sintering at 1200 °C for 30 min. The corresponding SAED patterns for each specimen are shown in Figs. 8(b) and 8(e), and the detailed zone axis and lattice plane information are summarized in Table S4 in the ESM. The 4Fe-8YSZ-D specimen was analyzed along the [$\bar{1}$12] zone axis, and the interplanar spacings of the observed ($\bar{1}1\bar{1}$) and (220) planes were measured to be 0.28 and 0.18 nm, respectively. The interplanar spacing in a cubic crystal structure is calculated using this equation $d_{hkl} = a/\sqrt{h^2 + k^2 + l^2}$, where a is the lattice parameter. h, k, and l are the Miller indices representing the orientation of the crystallographic plane. Based on a reference lattice constant of 0.514 nm [55], the calculated interplanar spacings for the ($\bar{1}1\bar{1}$) and (220) planes are 0.297 and 0.182 nm, respectively. The experimentally measured values were either slightly smaller or comparable, which is consistent with the typical lattice parameter of 8YSZ reported in Ref. [55]. In contrast, the 4Fe-8YSZ-Y specimen was analyzed along the [011] zone axis. As shown in Fig. 8(e), the interplanar spacings of the ($\bar{2}00$) planes were measured to be 0.263 and 0.258 nm. According to the relation $d_{(\bar{2}00)} = a/2$, these values correspond to lattice parameters of 0.526 and 0.516 nm, respectively, both of which are larger than the commonly reported value of approximately 0.513 nm for 8YSZ [55]. A comparison of the lattice plane characteristics between the two specimens shows that 4Fe-8YSZ-D exhibited interplanar spacings similar to or slightly smaller than the reference lattice parameter, whereas 4Fe-8YSZ-Y showed an increased value. This difference is attributed to lattice expansion induced by the elevated concentration of Y^{3+} ions supplied by the $Y(NO_3)_3{\cdot}6H_2O$ hydrate. Figure S8 in the ESM presents the TEM/EDS point analysis of 4Fe-8YSZ-D and 4Fe-8YSZ-Y after sintering at 1200 °C for 30 min. According to the point scan results, the 4Fe-8YSZ-Y specimen exhibited a significantly higher yttrium content near the grain boundaries, with a Y/Zr atomic ratio of approximately 28.05 at%. This result is consistent with the lattice expansion observed in Fig. 8(e) and supports the conclusion that the $Y(NO_3)_3$ solution contributed to enhanced yttrium incorporation within the YSZ structure. Figures 8(c) and 8(f) show the XPS O 1s spectra of the 4Fe-8YSZ-D and 4Fe-8YSZ-Y specimens, respectively, after CSP and subsequent CSP + CS treatment (sintered at 1200 °C for 30 min). Due to the surface-sensitive nature of XPS, the O 1s analysis is interpreted in terms of relative near-surface chemical states rather than bulk defect concentrations. According to the deconvolution results, the peak located near 529 eV corresponds to lattice oxygen (O_L), and the peak at approximately 531 eV, often associated with oxygen

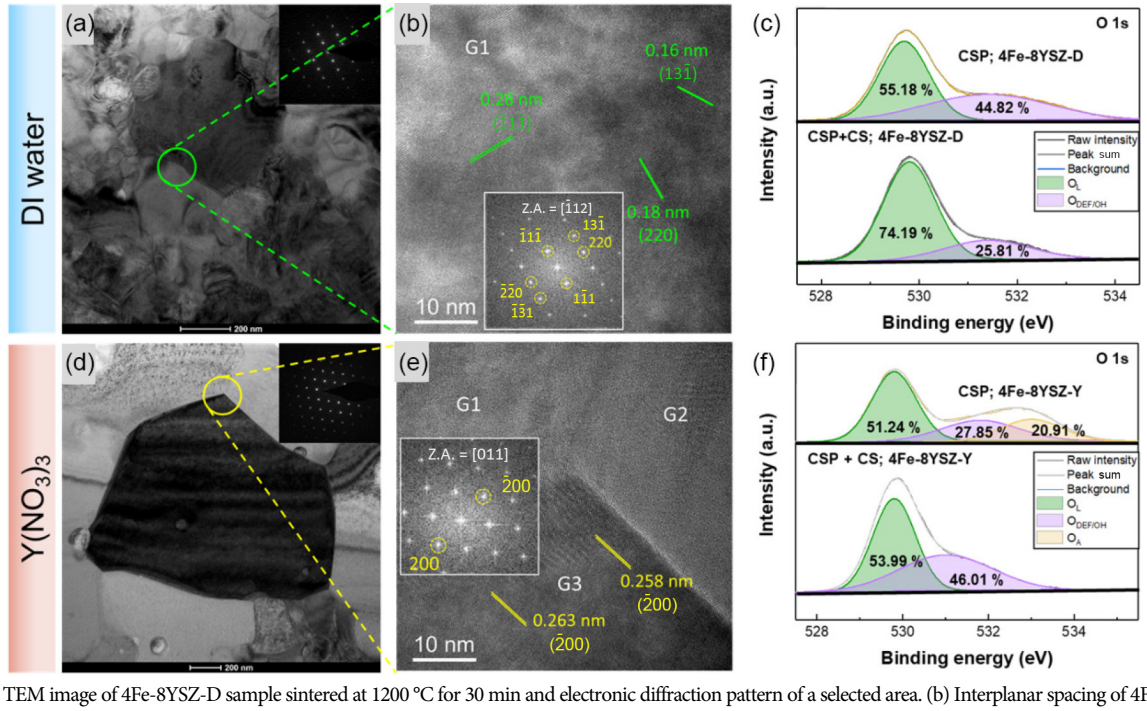

Fig. 8 (a) TEM image of 4Fe-8YSZ-D sample sintered at 1200 °C for 30 min and electronic diffraction pattern of a selected area. (b) Interplanar spacing of 4Fe-8YSZ-D measured from high-resolution TEM image. (c) O 1s XPS spectrum of 4Fe-8YSZ-D sample after sintering at 1200 °C for 30 min. (d) TEM image of 4Fe-8YSZ-Y sample sintered at 1200 °C for 30 min and electronic diffraction pattern of a selected area. (e) Interplanar spacing of 4Fe-8YSZ-Y measured from high-resolution TEM image. (f) O 1s XPS spectra of 4Fe-8YSZ-Y sample after sintering at 1200 °C for 30 min. O_L denotes lattice oxygen, $O_{DEF/OH}$ represents defective or surface-adsorbed oxygen species, and O_A corresponds to adsorbed oxygen in (c, f). Values represent relative spectral fractions, not absolute defect concentrations.

清華大学出版社 Tsinghua University Press | SciOpen

vacancies, cannot be unambiguously assigned in ambient-exposed samples due to the overlap with surface hydroxyl groups (e.g., O–H bonding) and other oxygen-deficient surface species. Therefore, this component is denoted here as defect/hydroxyl-related oxygen ($O_{DEF/OH}$). The higher binding energy peak at approximately 533 eV is generally attributed to weakly bound or adsorbed oxygen species (O_A) [56].

Figure S9 in the ESM shows the XPS analysis of the as-received 4Fe-8YSZ powder, which consists of 4.48% adsorbed oxygen (O_A), 45.18% $O_{DEF/OH}$, and 50.34% O_L. In contrast, the CSP-processed 4Fe-8YSZ-D specimen (Fig. 8(c)) exhibited no detectable O_A component within the fitting resolution, whereas the 4Fe-8YSZ-Y specimen (Fig. 8(f)) showed an increased O_A fraction of 20.91%. After subsequent sintering at 1200 °C for 30 min, the 4Fe-8YSZ-D sample (Fig. 8(c)) exhibited 25.81% $O_{DEF/OH}$ and 74.19% O_L, while the 4Fe-8YSZ-Y sample (Fig. 8(f)) showed 46.01% $O_{DEF/OH}$ and 53.99% O_L. These values represent relative surface spectral components and should not be interpreted as defect fractions. It is important to note that XPS is a surface-sensitive technique; thus, these values reflect the chemical states of the near-surface region rather than the bulk oxygen vacancy concentration. Nevertheless, the variation in the relative area of the 531 and 533 eV components indicates distinct surface adsorption behaviors and surface chemical environments between the two samples.

Table 2 lists the results of the Vickers hardness measurements. The comparison between 8YSZ-D and 4Fe-8YSZ-D isolates the effect of Fe_2O_3 under identical CSP solvent conditions, whereas the comparison between 4Fe-8YSZ-D and 4Fe-8YSZ-Y isolates the effect of CSP solvent chemistry at a fixed Fe_2O_3 level. To interpret the mechanical behavior, the hardness and indentation fracture toughness values must be considered in relation to grain size, residual porosity, grain-boundary chemistry, and crack propagation path, rather than as isolated numerical values. In ceramics consolidated via CSP pretreatment, the grain-boundary structure and defect chemistry can strongly influence the crack-tip stress distribution and deformation accommodation. In this study, the Vickers hardness was calculated according to a standard method using Eq. (4): H_v was determined as Eq. (4):

$$H_v = \frac{1.854P}{d^2} \tag{4}$$

where P is the applied load on the indenter (19.61 N), and d is the diagonal indentation. As a result, the 8YSZ-D specimen processed by CSP using DI water without Fe_2O_3 addition exhibited a Vickers hardness of 11.24 GPa. Among the Fe_2O_3-added samples, 4Fe-8YSZ-D (using DI water) showed a hardness of 13.88 GPa, while 4Fe-8YSZ-Y (using the $Y(NO_3)_3$ solution) exhibited the highest value of 14.99 GPa. This value surpasses those reported in previous works [11,13,20,41,57–61]. Compared to a previously reported hardness of 13.6 GPa for YSZ samples fabricated via a similar CSP+CS route [41]. The 4Fe-8YSZ-Y specimen demonstrated an improvement of approximately 10.22%. Furthermore, this value is also higher than those obtained by conventional sintering at higher temperatures.

The hardness enhancement correlates four coupled microstructural factors: fine grain size with high density (residual porosity) and grain-boundary chemistry. This study exhibits a smaller grain size than previous studies with higher sintering temperatures and longer sintering times [20,57,58]. K_{IC} values were calculated for each specimen using Anstis's equation (Eq. (5)) based on the radial crack lengths generated during Vickers hardness testing (Fig. S10 in the ESM). The results were compared as a function of sintering temperature in Fig. 9(f), along with previously reported values from the literature (represented by gray hexagons, squares, triangles, circles, diamonds and pentagons). K_{IC} was expressed as Eq. (5):

$$K_{IC} = 0.016\left(\frac{E}{H_v}\right)^{1/2}\left(\frac{P}{C^{3/2}}\right) \tag{5}$$

where E is Young's modulus, which is 220 GPa [11], and C is the linear dimension of the radial cracks. The fracture toughness values for 8YSZ-D, 4Fe-8YSZ-D, and 4Fe-8YSZ-Y were calculated to be 3.49, 5.56, and 2.96 MPa·m$^{1/2}$, respectively. The parameters

Table 2 H_v and K_{IC} values of sintered 8YSZ-D, 4Fe-8YSZ-D and 4Fe-8YSZ-Y samples

Sample	CSP+CS (CS: 1200 °C, 30 min)	
	H_v (GPa)	K_{IC} (MPa·m$^{1/2}$)
8YSZ-D	11.24±0.20	3.49±0.14
4Fe-8YSZ-D	13.88±1.29	5.56±0.27
4Fe-8YSZ-Y	14.99±0.37	2.96±0.10

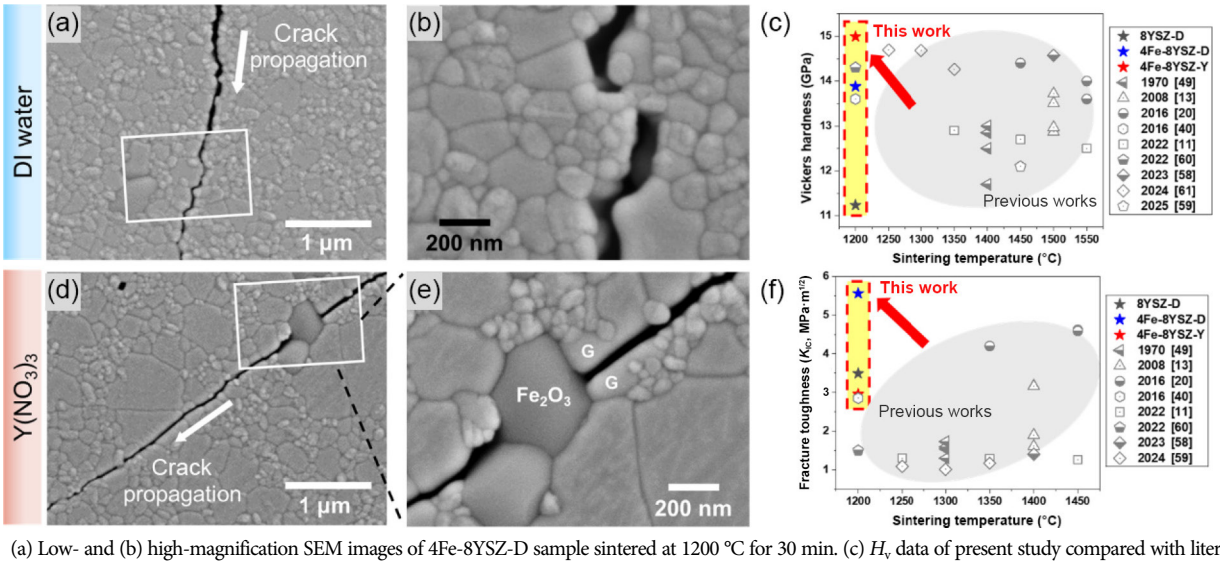

Fig. 9 (a) Low- and (b) high-magnification SEM images of 4Fe-8YSZ-D sample sintered at 1200 °C for 30 min. (c) H_v data of present study compared with literature. (d) Low- and (e) high-magnification SEM images of 4Fe-8YSZ-Y sample sintered at 1200 °C for 30 min. (f) K_{IC} data of present study compared with values reported in previous works.

used in the calculations are summarized in Table S5 in the ESM. In this study, the influence of Fe_2O_3 addition on the H_v and K_{IC} varied depending on the solvent. While the 4Fe-8YSZ-D specimen exhibited simultaneous improvements in both hardness and toughness due to Fe_2O_3 doping, the 4Fe-8YSZ-Y specimen showed the highest hardness but a decreased fracture toughness. The reduced fracture toughness of 4Fe-8YSZ-Y is primarily attributed to the pronounced bimodal grain size distribution (AGG) and the associated transition toward more transgranular crack segments (Figs. 9 and S11 in the ESM). The XPS O 1s spectra indicate a higher fraction of $O_{DEF/OH}$ for 4Fe-8YSZ-Y. This observation suggests differences in surface chemistry/adsorption state, but it should not be interpreted as a quantitative measure of bulk oxygen-vacancy concentration [62]. The observed variations in hardness and fracture toughness should be interpreted in conjunction with the microstructural features shown in Fig. 9. Figures 9(a) and 9(d) present the microstructures of the 4Fe-8YSZ-D and 4Fe-8YSZ-Y specimens, respectively, after sintering at 1200 °C for 30 min. A significant difference in the frequency of abnormal grain occurrence is evident between the two samples, with the 4Fe-8YSZ-Y specimen exhibiting a much higher number of selectively coarsened abnormal grains. Further analysis of the average grain size and grain size distribution is provided in Fig. S11 in the ESM. While the average grain size of the 4Fe-8YSZ-Y specimen was calculated to be 120.68 nm (compared to 88.42 nm for 8YSZ-D), the distribution reveals a significant bimodal character due to AGG [63]. The microstructure consists of a fine matrix and localized coarse grains. Such heterogeneous microstructural features are likely to act as initiation sites for crack formation and propagation. Therefore, the reduced fracture toughness of 4Fe-8YSZ-Y is attributed to stress concentrations arising from the bimodal grain size distribution and the associated shift toward more transgranular crack segments (Figs. 9 and S11 in the ESM). Although Fe-containing particles may locally induce crack deflection, this potential toughening contribution is outweighed by AGG-induced transgranular fracture in the Y-treated sample. In contrast, the 4Fe-8YSZ-D specimen exhibited superior fracture toughness, which can be ascribed to the relatively limited influence of these factors. Figure 9 reveals distinct differences in crack propagation behavior depending on the type of solvent used. In the 4Fe-8YSZ-D specimen, cracks primarily propagated along the grain boundaries, indicating intergranular fracture behavior (Figs. 9(a) and 9(b). In contrast, the 4Fe-8YSZ-Y specimen exhibited transgranular fracture characteristics when the $Y(NO_3)_3$ solution was used (Figs. 9(d) and 9(e)).

This distinction was attributed to differences in the average grain size and grain boundary strength induced by the solvent during sintering. In addition, Fe_2O_3 particles in the 4Fe-8YSZ-Y specimen were observed to disrupt the crack propagation path, promoting crack deflection and energy dispersion. A similar mechanism from the Fe_2O_3 particles is presumed to operate in the 4Fe-8YSZ-D specimen as well. Figure S12 in the ESM shows SEM images of the fracture surfaces of both specimens. The 4Fe-8YSZ-D sample (Figs. S12(a) and S12(b) in the ESM) predominantly exhibited intergranular fracture, whereas the 4Fe-8YSZ-Y sample (Figs. S12(c) and S12(d) in the ESM) showed transgranular fracture as the dominant mode. Figure S13 in the ESM presents a combined comparison of the Vickers hardness and fracture toughness values measured in this study for 4Fe-8YSZ-Y (red star), 4Fe-8YSZ-D (blue star), and 8YSZ-D (black star) with those reported in previous studies, represented by hexagon [41], square [11], filled left triangle [57], half-filled circle [20], triangle [13], half-filled diamond [58], half-filled pentagon [60], and diamond [61]. As confirmed in Table 2, the 4Fe-8YSZ-Y specimen exhibited the highest hardness, while the 4Fe-8YSZ-D specimen showed the highest fracture toughness; both values exceeded those reported in the literature. These results provide important insight into the influence of Fe_2O_3 addition and the type of solvent used during CSP on the mechanical properties of 8YSZ. In particular, the $Y(NO_3)_3$ solution employed in this study effectively promoted densification during CSP and subsequent high-temperature sintering, resulting in enhanced density and improved hardness. The mechanical performance observed in this study can be understood through a hierarchical causal sequence of processing–microstructure–fracture mechanics rather than by a single dominant factor.

First, the processing history defined by CSP pretreatment and solvent chemistry governs the resulting microstructure. The relatively low sintering temperature (1200 °C) following CSP effectively suppressed grain coarsening, preserving a fine and largely uniform grain structure (4Fe-8YSZ-D; Fig. S11 in the ESM). This refinement, combined with high densification (relative density > 98%), increases the grain-boundary area and resistance to localized contact deformation, leading to a high hardness consistent with the grain refinement strengthening trend. Second, fracture behavior is controlled by microstructural heterogeneity rather than phase transformation, as the matrix is predominantly cubic fluorite. Dispersed Fe-containing regions and grain boundaries act as obstacles to crack propagation. In the DI water-processed specimen, the finer and more homogeneous microstructure promotes intergranular crack deflection, resulting in increased crack path tortuosity and higher fracture energy dissipation. In contrast, the $Y(NO_3)_3$-treated specimen exhibits abnormal grain growth (Fig. S11 in the ESM), where coarse grains facilitate more transgranular fracture segments (Fig. 9), reducing the crack deflection efficiency. Thus, solvent chemistry functions as an interface-engineering parameter that determines grain size homogeneity and crack path geometry, which in turn governs the balance between hardness and fracture toughness. Because the Fe_2O_3 content and thermal schedule are identical for 4Fe-8YSZ-D and 4Fe-8YSZ-Y, the observed differences in grain growth mode and crack-path geometry are attributed to the interfacial chemical state established during the CSP stage rather than to Fe-assisted high-temperature sintering.

Finally, regarding the reliability of the mechanical data, indentation tests were performed under a load of 19.61 N (2 kgf), which lies well above the low-load regime (< 5 N) where indentation size effect (ISE)-related overestimation of toughness is most severe. At this load, well-developed median/radial cracks satisfying the validity criterion (c > 2a) were obtained. Because identical testing conditions were used for all samples, ISE-related artifacts were minimized for comparative analysis. Therefore, the reported values represent comparative indentation fracture resistance rather than intrinsic long-crack toughness, but they remain valid for assessing relative toughening trends among CSP-processed materials.

4 Conclusions

This study demonstrates that the densification and mechanical performance of 8YSZ can be effectively tailored through a stage-resolved combination of Fe_2O_3 addition and CSP pretreatment. *In situ* dilatometry revealed that CSP induces measurable densification at the low-temperature stage via particle rearrangement and solvent-assisted transport, thereby establishing a high green density prior to high-temperature sintering. In contrast, Fe_2O_3 primarily influences the subsequent thermal stage by accelerating mass transport and diffusion kinetics.

Solvent chemistry during CSP was identified as a key microstructure-control parameter. The $Y(NO_3)_3$-treated specimen achieved higher hardness but exhibited reduced fracture toughness, primarily due to abnormal grain growth, with XPS indicating differences in near-surface chemical states rather than bulk defect concentrations. Conversely, the DI water-treated specimen maintained a finer and more uniform microstructure, promoting crack deflection and resulting in a more balanced combination of hardness and toughness. These findings show that solvent selection enables control over grain growth behavior, crack propagation mode, and the resulting hardness–toughness trade-off.

Finally, the *in situ* shrinkage monitoring approach provides both densification kinetics and mechanistic insight by separating pressure- and temperature-assisted densification within the CSP stage while enabling interpretation of the subsequent thermally activated diffusion stage. This framework offers a practical pathway for stage-specific microstructure and property tuning in low-temperature-assisted ceramic sintering systems.

Acknowledgements

This work was supported by the National Research Foundation of Korea (NRF) grant funded by the Korea government (Ministry of Science and ICT, MSIT, RS-2024-00347338) and by the Global-Learning & Academic Research Institution for Master's·PhD Students and the Postdocs (LAMP) Program of the National Research Foundation of Korea (NRF) grant funded by the Ministry of Education (MOE, No. RS-2024-00444460). Additionally, this work was supported by the Korea Planning & Evaluation Institute of Industrial Technology (KEIT) grant funded by the Ministry of Trade, Industry, and Energy (MOTIE, No. RS-2024-00469379). CAR and SM are supported by the National Science Foundation (No. DMR 2202525).

Availability of data and materials

The data that support the findings of this study are available from the corresponding author upon reasonable request.

Competing interests

The authors have no competing interests to declare that are relevant to the content of this article.

Electronic Supplementary Material

Supplementary material is available in the online version of this article at https://doi.org/10.26599/JAC.2026.9221278.

References

[1] Kareem SJ, Asaad MW, Al-Ethari H. Enhancement of tribological properties of carbide cutting tools by ceramic coating deposition. *Heat Treat Surf Eng* 2024, **6**: 2331865.

[2] Simonenko NP, Simonenko EP, Mokrushin AS, *et al.* Thin films of the composition 8% Y_2O_3–92% ZrO_2 (8YSZ) as gas-sensing materials for oxygen detection. *Russ J Inorg Chem+* 2017, **62**: 695–701.

[3] Dong YH, Liu ZY, Qiu GX, *et al.* A limiting current oxygen sensor with 8YSZ solid electrolyte and $(8YSZ)_{0.9}(CeO_2)_{0.1}$ dense diffusion barrier. *J Alloys Compd* 2021, **885**: 160903.

[4] Wang L, Wang Y, Sun XG, *et al.* Thermal shock behavior of 8YSZ and double-ceramic-layer $La_2Zr_2O_7$/8YSZ thermal barrier coatings fabricated by atmospheric plasma spraying. *Ceram Int* 2012, **38**: 3595–3606.

[5] Wang YZ, Li JL, Liu HZ, *et al.* Study on thermal resistance performance of 8YSZ thermal barrier coatings. *Int J Therm Sci* 2017, **122**: 12–25.

[6] Zhou FF, Wang S, Xu BS, *et al.* Nanomechanical properties of plasma-sprayed nanostructured and conventional 8YSZ thermal barrier coatings. *Ceram Int* 2022, **48**: 37483–37487.

[7] Singhal SC. Solid oxide fuel cells for stationary, mobile, and military applications. *Solid State Ionics* 2002, **152**: 405–410.

[8] Van Gestel T, Sebold D, Buchkremer HP. Processing of 8YSZ and CGO thin film electrolyte layers for intermediate- and low-temperature SOFCs. *J Eur Ceram Soc* 2015, **35**: 1505–1515.

[9] Khan MS, Lee SB, Song RH, *et al.* Fundamental mechanisms involved in the degradation of nickel-yttria stabilized zirconia (Ni-YSZ) anode during solid oxide fuel cells operation: A review. *Ceram Int* 2016, **42**: 35–48.

[10] Casolco SR, Xu J, Garay JE. Transparent/translucent polycrystalline nanostructured yttria stabilized zirconia with varying colors. *Scripta Mater* 2008, **58**: 516–519.

[11] Chen PH, Li XY, Tian F, *et al.* Fabrication, microstructure, and properties of 8 mol% yttria-stabilized zirconia (8YSZ) transparent ceramics. *J Adv Ceram* 2022, **11**: 1153–1162.

[12] Dahl P, Kaus I, Zhao Z, *et al.* Densification and properties of zirconia prepared by three different sintering techniques. *Ceram Int* 2007, **33**: 1603–1610.

[13] Mazaheri M, Zahedi AM, Hejazi MM. Processing of nanocrystalline 8 mol% yttria-stabilized zirconia by conventional, microwave-assisted and two-step sintering. *Mater Sci Eng A* 2008, **492**: 261–267.

[14] Mazaheri M, Hesabi ZR, Golestani-Fard F, *et al.* The effect of conformation method and sintering technique on the densification and grain growth of nanocrystalline 8 mol% yttria-stabilized zirconia. *J Am Ceram Soc* 2009, **92**: 990–995.

[15] Kim BN, Suzuki TS, Morita K, *et al.* Densification kinetics during isothermal sintering of 8YSZ. *J Eur Ceram Soc* 2016, **36**: 1269–1275.

[16] Irshad M, Siraj K, Raza R, *et al.* Evaluation of densification effects on the properties of 8 mol% yttria stabilized zirconia electrolyte synthesized by cost effective coprecipitation route. *Ceram Int* 2021, **47**: 2857–2863.

[17] Tekeli S, Gürü M, Sag˙lam OE. Densification and grain-growth behavior of various amounts of SiO_2 doped 8YSCZ/SiO_2 composites. *Mater Manuf Process* 2007, **22**: 710–714.

[18] Zhang TS, Chan SH, Wang W, *et al.* Effect of Mn addition on the densification, grain growth and ionic conductivity of pure and SiO_2-containing 8YSZ electrolytes. *Solid State Ionics* 2009, **180**: 82–89.

[19] Batista RM, Muccillo ENS. Densification and grain growth of 8YSZ containing NiO. *Ceram Int* 2011, **37**: 1047–1053.

[20] Chong FD, Tan CY, Singh R, *et al.* Effect of manganese oxide on the sinterability of 8 mol% yttria-stabilized zirconia. *Mater Charact* 2016, **120**: 331–336.

[21] Guo FW, Xiao P. Effect of Fe_2O_3 doping on sintering of yttria-stabilized zirconia. *J Eur Ceram Soc* 2012, **32**: 4157–4164.

[22] Lin C, Li HY, Huang YM, *et al.* Phase evolution and enhanced sinterability of cold sintered Fe_2O_3-doped 8YSZ. *Ceram Int* 2020, **46**: 14217–14223.

[23] Khor KA, Gu YW. Hot isostatic pressing of plasma sprayed yttria-stabilized zirconia. *Mater Lett* 1998, **34**: 263–268.

[24] Goldstein A, Travitzky N, Singurindy A, *et al.* Direct microwave sintering of yttria-stabilized zirconia at 2.45 GHz. *J Eur Ceram Soc* 1999, **19**: 2067–2072.

[25] Rajeswari K, Suresh MB, Chakravarty D, *et al.* Effect of nano-grain size on the ionic conductivity of spark plasma sintered 8YSZ electrolyte. *Int J Hydrogen Energ* 2012, **37**: 511–517.

[26] Paygin V, Stepanov S, Dvilis E, *et al.* Effect of technological parameters on optical and mechanical properties of spark plasma sintered transparent YSZ ceramics. *Ceram Int* 2021, **47**: 11169–11175.

[27] Taguchi K, Ishino Y, Tokunaga T, *et al.* Near complete densification of flash sintered 8YSZ: Controlled shrinkage rate effects. *J Eur Ceram Soc* 2021, **41**: 4567–4571.

[28] Wang SF, Mishra TP, Deng YB, *et al.* Experimental and numerical studies of densification and grain growth of 8YSZ during flash sintering. *Adv Eng Mater* 2023, **25**: 2201744.

[29] Ralph JM, Schoeler AC, Krumpelt M. Materials for lower temperature solid oxide fuel cells. *J Mater Sci* 2001, **36**: 1161–1172.

[30] Batista RM, Muccillo ENS. Structure, microstructure and electrical conductivity of 8YSZ containing NiO. *Ceram Int* 2011, **37**: 1929–1934.
[31] Baker A, Guo HZ, Guo J, *et al.* Utilizing the cold sintering processfor flexible–printable electroceramic device fabrication. *J Am Ceram Soc* 2016, **99**: 3202–3204.
[32] Guo J, Baker AL, Guo HZ, *et al.* Cold sintering process: A new era for ceramic packaging and microwave device development. *J Am Ceram Soc* 2017, **100**: 669–677.
[33] Jiang XP, Zhu GS, Xu HR, *et al.* Preparation of high density ZnO ceramics by the cold sintering process. *Ceram Int* 2019, **45**: 17382–17386.
[34] Nur K, Mishra TP, da Silva JGP, *et al.* Influence of powder characteristics on cold sintering of nano-sized ZnO with density above 99 %. *J Eur Ceram Soc* 2021, **41**: 2648–2662.
[35] Fanghanel J, Yokomizo S, Funahashi S, *et al.* Cold sintering of nickel manganese oxide for thermistor fabrication. *J Mater Chem A* 2024, **12**: 33984–33990.
[36] Wang DX, Guo HZ, Morandi CS, *et al.* Cold sintering and electrical characterization of lead zirconate titanate piezoelectric ceramics. *APL Mater* 2018, **6**: 016101.
[37] Palneedi H, Sharief P, Hong SM, *et al.* Densification and grain growth in ceramics fabricated by cold sintering: A review on the effect of process parameters. *J Am Ceram Soc* 2026, **109**: 70268.
[38] Lai QY, Chen J, Chang F, *et al.* Cold sintering process assisted sintering for 8YSZ ceramic: A way of achieving high density and electrical conductivity at a reduced sintering temperature. *Ceram Int* 2023, **49**: 14744–14749.
[39] Grimes C, Button CA, Zhao A, *et al.* Cold sintering of α-alumina using functionalized boehmite: A cost-effective approach to reduce sintering temperature. *J Am Ceram Soc* 2025, **108**: 70208.
[40] Guo HZ, Baker A, Guo J, *et al.* Protocol for ultralow-temperature ceramic sintering: An integration of nanotechnology and the cold sintering process. *ACS Nano* 2016, **10**: 10606–10614.
[41] Guo HZ, Bayer TJM, Guo J, *et al.* Cold sintering process for 8 mol% Y_2O_3-stabilized ZrO_2 ceramics. *J Eur Ceram Soc* 2017, **37**: 2303–2308.
[42] Guo HZ, Bayer TJM, Guo J, *et al.* Current progress and perspectives of applying cold sintering process to ZrO_2-based ceramics. *Scripta Mater* 2017, **136**: 141–148.
[43] Ullah A, Palneedi H, Jeon SC. Enhanced densification and dielectric properties of $BaTiO_3$ through a cold-sintering pre-treatment. *J Eur Ceram Soc* 2025, **45**: 117036.
[44] Huang YM, Huang KM, Zhou SY, *et al.* Influence of incongruent dissolution-precipitation on 8YSZ ceramics during cold sintering process. *J Eur Ceram Soc* 2022, **42**: 2362–2369.
[45] Denis Y, Philippot G, Roitero E, *et al.* Cold sintering of zirconia and yttria-stabilized zirconia from reactive hydroxides precursors. *J Eur Ceram Soc* 2025, **45**: 117650.
[46] Floyd R, Lowum S, Maria JP. Instrumentation for automated and quantitative low temperature compaction and sintering. *Rev Sci Instrum* 2019, **90**: 055104.
[47] Bang SH, Ndayishimiye A, Randall CA. Anisothermal densification kinetics of the cold sintering process below 150 °C. *J Mater Chem C* 2020, **8**: 5668–5672.
[48] Maier RA. *In situ* observation of the multistep process of cold sintering. *J Am Ceram Soc* 2024, **107**: 6544–6553.
[49] Zhang JX, Feng ZY, Song JH, *et al.* Crystal defects and phase transitions of nanocrystalline yttria-stabilised zirconia induced by high-energy ball milling. *Ceram Int* 2021, **47**: 16432–16440.
[50] Washburn EW. The dynamics of capillary flow. *Phys Rev* 1921, **17**: 273–283.
[51] Guo HZ, Baker A, Guo J, *et al.* Cold sintering process: A novel technique for low-temperature ceramic processing of ferroelectrics. *J Am Ceram Soc* 2016, **99**: 3489–3507.
[52] Young WS, Cutler IB. Initial sintering with constant rates of heating. *J Am Ceram Soc* 1970, **53**: 659–663.
[53] Matsui K. Sintering kinetics at constant rates of heating: Mechanism of silica-enhanced sintering of fine zirconia powder. *J Am Ceram Soc* 2008, **91**: 2534–2539.
[54] Momjian S, Mauro JC, Randall CA. Non-equilibrium thermodynamics and kinetics of the sintering process: A relaxation model describing cold sintering. *J Am Ceram Soc* 2025, **108**: 70180.
[55] Ingel RP, Lewis D. Lattice parameters and density for Y_2O_3-stabilized ZrO_2. *J Am Ceram Soc* 1986, **69**: 325–332.
[56] Liu Y, Zuo LW, Jiang C, *et al.* Composite electrolyte used for low temperature SOFCs to work at 390 ℃. *iScience* 2023, **26**: 107002.
[57] Kwon NH, Kim GH, Song HS, *et al.* Synthesis and properties of cubic zirconia–alumina composite by mechanical alloying. *Mater Sci Eng A* 2001, **299**: 185–194.
[58] Li YP, Sun HQ, Song J, *et al.* The influence of hafnium removal on the microstructure and properties of 8YSZ ceramics. *Ceram Int* 2023, **49**: 29564–29572.
[59] Chen YP, Wang Y, Ma T, *et al.* 8 mol% Y_2O_3-stabilized zirconia (8YSZ) transparent ceramics with high optical and mechanical performance through YF_3 sintering additive. *J Eur Ceram Soc* 2025, **45**: 117621.
[60] Akhlaghi O, Camposilvan E, Goharibajestani Z, *et al.* Transparent high-strength nanosized yttria stabilized zirconia obtained by pressure-less sintering. *J Eur Ceram Soc* 2022, **42**: 7187–7195.
[61] Zhou D, Ding CZ, Han WJ, *et al.* Low-temperature fabrication of zirconia transparent ceramics via hydrothermal nanopowder. *Ceram Int* 2024, **50**: 49210–49216.
[62] Morales M, Roa JJ, Capdevila XG, *et al.* Mechanical properties at the nanometer scale of GDC and YSZ used as electrolytes for solid oxide fuel cells. *Acta Mater* 2010, **58**: 2504–2509.
[63] Moon KS, Kang SL. Coarsening behavior of round-edged cubic grains in the $Na_1/2Bi_1/2TiO_3$–$BaTiO_3$ System. *J Am Ceram Soc* 2008, **91**: 3191–3196.